ChemComm

Check for updates

Mn-based tunnel-structured $Na_{0.44}MnO_2$ cathode materials for high-performance sodium-ion batteries: electrochemical mechanism, synthesis and modifications

Dong Wang, Liumei Teng and Weizao Liu 🆔 *

Sodium-ion batteries (SIBs) have emerged as promising and mature alternatives to lithium-ion batteries (LIBs) in the post-LIB era, necessitating the development of cost-effective and high-performance cathode materials. The unique crystal texture of Mn-based tunnel-structured cathode materials offers outstanding cycling stability, rate capability and air stability, making them a highly attractive option for sodium-ion storage applications. This comprehensive review summarizes recent advancements in the understanding of sodium-ion storage mechanism, synthesis techniques, and modification strategies for Mn-based tunnel-structured cathode materials, thereby significantly contributing to the advancement of high-performance cathodes for SIBs.

1. Introduction

Sodium-ion batteries (SIBs), characterized by their abundant resources, high performance, and low cost, are considered a promising complementary technology to lithium-ion batteries (LIBs). This makes SIBs particularly suitable for grid-scale energy storage, offering significant potential for broad applications.[1–6] Over the past decade, significant progress has been made in the development of electrochemical energy storage technologies for SIBs. Both fundamental research and commercialization efforts have gained significant momentum, leading to promising advancements in this rapidly evolving field.[7] Continuous innovations in material iteration and device engineering optimization for SIBs further enhance their potential for future growth in the energy storage market. In the SIB system, the choice of cathode material is a critical factor that influences both battery performance and cost.[8] One key advantage of SIBs is their ability to utilize a wide range of cathode materials. Currently, a series of cathode materials have been specifically developed for SIBs, encompassing transition metal oxides,[9–12] polyanionic compounds,[13] Prussian blue analogues (PBAs),[14] and organic cathode materials.[15] This diverse array enables researchers and engineers to tailor the overall battery performance according to specific requirements, such as high energy density, long cycle life, or fast-charging capabilities.[16]

One of the key challenges in advancing SIB technologies lies in the enhancement and fine-tuning of cathode materials.

College of Materials Science and Engineering, Chongqing University, Chongqing, 400044, China. E-mail: liuwz@cqu.edu.cn

These materials must be optimized to effectively accommodate sodium ions while facilitating rapid and reversible sodium-ion insertion/extraction process.[17–20] Ensuring cycling stability is crucial for the practical implementation of SIBs in large-scale energy storage systems. Due to their advantages of abundant manganese reserves, environment friendliness and low cost, the study of Na–Mn–O cathode materials has become a key focus in the research of SIBs.[21] The manganese (Mn)-based layer-structured cathode materials can be further categorized into P2-$Na_{0.67}MnO_2$ and O3-$NaMnO_2$ phase structures based on the stacking sequences of oxygen atoms and the positions occupied by sodium ions within the manganate-based oxide structure.[22] Here, P and O denote the coordination environment of Na^+ in trigonal prismatic and octahedral configurations, respectively. Moreover, 2 and 3 represent the number of transition metal layers within each cyclic unit of the layered structure.[23] Among these manganese oxides, the Mn-based tunnel-structured cathode material $Na_4Mn_9O_{18}$ ($Na_{0.44}MnO_2$) has been extensively researched as a promising cathode material for SIBs due to its unique S-type tunnel structure, which facilitates rapid de-embedding of sodium ions, along with outstanding cycling stability and superior rate capability than layer-type cathode.[24–26] This type of Mn-based tunnel structure material was first reported by Parant *et al.* in 1971,[27] but it was not until 1994 that Doeff and his colleagues studied this tunnel-type structure as an electrode material for electrochemical sodium-ion de-/intercalation process.[28] The Mn-based tunnel crystal structure depicted in Fig. 1(a) predominantly comprises five distinct manganese-ion sites and three different sodium-ion sites. The $Na_{0.44}MnO_2$ exhibits the same crystal structure as $Na_4Mn_4Ti_5O_{18}$ and adopts an orthorhombic structure
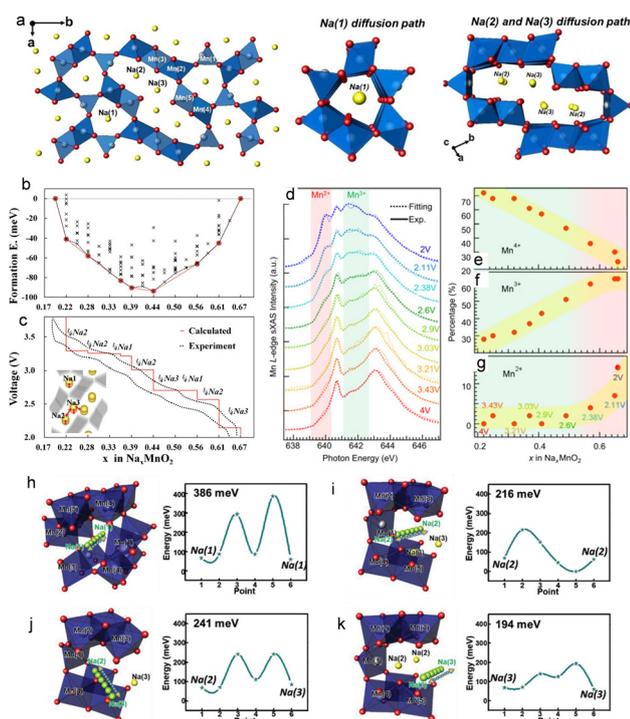
Fig. 1 (a) Crystal-structure diagram of Mn-based tunnel-structure $Na_{0.44}MnO_2$. Reproduced with permission from ref. 40, Copyright (2021), Wiley-VCH. (b) Seven stable intermediate phases during the cycles of Na_xMnO_2 ($x = 0.19–0.44$) obtained from the calculated formation energies. (c) Contrasting graph of the calculated voltage profile along the minimum energy path on formation energies and the initial charging/discharging curve from experimental data. Reproduced with permission from ref. 41, Copyright (2012), the American Chemical Society. (d) Mn L-edge sXAS data collected on Na_xMnO_2 cathode at different voltages. (e)–(g) Concentration evolution of Mn^{4+}, Mn^{3+} and Mn^{2+} at varying sodium-ion concentrations from Na_xMnO_2 cathode. Reproduced with permission from ref. 42, Copyright (2015), Elsevier. Sodium-ion diffusion energy barriers for the tunnel-structured $Na_{0.44}MnO_2$ demonstrated for the Na-site pairs (h) Na(1)–Na(1); (i) Na(2)–Na(2); (j) Na(2)–Na(3); and (k) Na(3)–Na(3). Reproduced with permission from ref. 43, Copyright (2020), Wiley-VCH.

arrangement (space group: *Pbam*). The Mn(1) and Mn(2) sites indicated are occupied by Mn^{3+}, while the remaining Mn(3), Mn(4), and Mn(5) sites are occupied by Mn^{4+}. The entire framework is composed of double and triple linear chain structures with shared edges of $MnO6$ octahedra, as well as a single chain structure with shared edges of $MnO5$ tetrahedra.[29–31] Through the interconnected angles of these polyhedra, adjacent chain structures combine to form a "pentagonal" one-dimensional tunnel configuration, along with another S-shaped two-dimensional tunnel configuration. The sodium-ion sites distributed within these two types of tunnel structures can be categorized into two groups: Na(1) site located within the pentagonal tunnel, and Na(2) and Na(3) sites belonging to the S-type tunnel.[32,33] Sodium ions at the Na(2) and Na(3) positions within the wide S-shaped tunnel structure exhibit rapid diffusion ability along the *c*-axis direction, while sodium ions within the smaller pentagonal tunnel are generally considered immobile under conventional electrochemical conditions. Consequently, there is limited availability for extracting sodium ions from this crystal structure, which restricts

its theoretical electrochemical capacity (121 mA h g^{-1}) as a high-energy-density electrode.[34,35] However, its exceptional sodium ion diffusion kinetics and structural stability continue to be extensively investigated in non-aqueous and aqueous SIBs.[36–39] The size of the tunnel should be adjusted to accommodate the requirements of Na$^+$ insertion/extraction, while Mn-based materials inevitably encounter Jahn–Teller distortion induced by Mn^{3+}. These factors contribute to structural deterioration and Mn dissolution of the tunnel structure cathode materials, resulting in low-rate performance and limited cycle stability.

Therefore, a comprehensive review is imperative to elucidate and summarize the electrochemical mechanism, synthesis methods, modification strategies, and other pertinent aspects of Mn-based tunnel structure cathode materials for SIBs. This will enable researchers in the field of energy storage materials to gain a lucid understanding of the research progress and future development directions in Mn-based tunnel structure cathode materials, thereby further advancing the fundamental investigation and industrialization of high-performance SIBs.

2. Sodium-ion storage mechanism

The unique atomic arrangement in the tunnel-type structure of Na–Mn–O contributes to its exceptional crystal structure stability, distinguishing it from layer-structure compounds, such as the P2-type layer or O3-type layer, which undergo significant cell volume expansion and eventually structure collapse, leading to inadequate cyclability.[7,44] Therefore, it is crucial to investigate the sodium-ion storage mechanism in Mn-based tunnel cathode materials despite their lower reversible capacity. The larger S-shaped tunnel structure has Na(2) and Na(3) sites that significantly contribute to the redox reaction during charge/discharge processes, while the smaller pentagram tunnel structure contains Na(1) sites where minimal sodium-ion insertion and de-intercalation occur electrochemically.[40] Mn ions exist in two distinct environments: all Mn^{4+} ions and half of the Mn^{3+} ions occupy octahedral sites (MnO6), while the remaining Mn^{3+} ions are situated within a square-pyramidal environment (MnO5). The crystal particle within this structure comprises both Mn^{3+} and Mn^{4+} oxidation states, which are charge-neutral as represented by the chemical composition $Na^+_4Mn^{3+}_4Mn^{4+}_5O^{2-}_{18}$. During the charging and discharging processes, the range of variation for the molar ratio of Na/TM primarily lies from 0.22 to 0.66. The charging process primarily involves the following chemical reactions: $Na_{0.44}MnO_2 - 0.22\ Na^+ - 0.22\ e^- \rightarrow Na_{0.22}MnO_2$. Conversely, the corresponding discharge process can be denoted as $Na_{0.44}MnO_2 + 0.22\ Na^+ + 0.22\ e^- \rightarrow Na_{0.66}MnO_2$.

Baudrin *et al.*[45] used the potentiostatic intermittent titration technique (PITT), along with *in situ* X-ray diffraction (*in situ* XRD) measurements, to clearly demonstrate the complexity of the sodium-ion insertion/de-insertion process. They observed at least six distinct biphasic phenomena in 2–3.8 V (*vs.* Na$^+$/Na) within a composition range of $0.18 < x < 0.64$ in the compound Na_xMnO_2. Kim *et al.*[41] conducted density functional theory (DFT) calculations to investigate the structural and

electrochemical properties of $Na_{0.44}MnO_2$ cathode material. They identified seven intermediate phases and two-phase reactions, which were consistent with the experimental data (Fig. 1(b) and (c)). Furthermore, they highlighted that despite the presence of Mn^{3+} ions throughout all electrochemical cycles, the crystal structure of $Na_{0.44}MnO_2$ does not undergo structural transformations due to its unique arrangement of an oxygen lattice along the *a*-axis rather than cubic close-packed layers. Additionally, they found that the migration of Mn ions into neighboring vacant sodium-ion sites is unfavorable, and structures with varying sodium-ion content ranging from 0.22 to 0.66 in the crystal structure are more energetically stable compared to nearby Na–Mn–O compounds. These factors contribute significantly to maintaining structural stability and ensuring superior cycling performance during the sodium-ion extraction/insertion processes for tunnel-structure cathode materials. Afterwards, Kim and his colleagues[46] further investigated the sodium-ion intercalation/de-intercalation behavior of $Na_{0.44}MnO_2$ tunnel-structure cathode materials by utilizing electrochemical impedance spectroscopy (EIS) measurements. They discovered that the apparent sodium-ion diffusion coefficients in organic electrolyte systems ranged from 5.75×10^{-16} to 2.14×10^{-14} cm^2 s^{-1}. Additionally, the CV curve exhibited at least six redox reaction processes that aligned with the corresponding charge/discharge curves. Aurbach *et al.*[43] combined various characterization methods, including X-ray diffraction data, 3D bond valence difference maps and X-ray diffraction data. The barrier-energy calculations of sodium diffusion were used to study the sodium-ion intercalation mechanism. The ion migration during the contributions of Na(2) and Na(3) sites in the S-shaped tunnel structure was further confirmed (Fig. 1(h)–(k)). In addition to investigating the evolution of the crystal structure within the bulk structure during the charging and discharging processes, comprehending the alterations in surface structure also plays a pivotal role in influencing electrochemical performance. Yang *et al.*[42] conducted an extensive analysis utilizing surface-sensitive soft X-ray absorption spectroscopy (sXAS) to quantitatively explore the transformation of Mn on the surface area of tunnel-structure cathode materials $Na_{0.44}MnO_2$ with varying potentials and electrochemical cycle numbers. They discovered that below an electrochemical potential of 2.6 V, the specific formation of Mn^{2+} occurs solely on the outside layer of crystal particles for 10 nm, which is not detected in the bulk material (Fig. 1(d)–(g)). Moreover, after prolonged cycles, some of these surface compounds, including Mn^{2+}, become electrochemically inactive, contributing to the degradation of discharge capacity.

The electrochemical sodium-ion storage mechanism of Mn-based tunnel structure cathode materials has been extensively investigated by researchers using *in/ex situ* characterization means and theoretical calculations. These studies have focused on understanding the electrochemistry behavior of Mn-based tunnel structure materials during the charge and discharge processes from the perspectives of crystal structure, local structure and electrochemical property. However, further attention can be given to the crystal structure and surface chemical environment evolution of cathode materials after long cycles and variations in sodium-ion transport channels in the tunnel-type crystal texture.

3. Material synthesis

Researchers have employed various synthesis methods to prepare Mn-based tunnel structure materials to investigate their sodium-ion storage properties and electrochemistry mechanism as a cathode in SIBs, including the high-temperature solid-phase method, sol–gel method, co-precipitation method,[47] and hydrothermal method. The following section presents the commonly utilized synthesis methods in Mn-based tunnel structure materials.

3.1 Solid-phase method

The high-temperature solid phase method is one of the common synthesis solutions for transition-metal-oxide cathode materials. The synthesis approach possesses the benefits of a straightforward procedure, convenient access to raw materials, manageable regulation of reaction conditions, and economical production expenses. Consequently, it has extensive application in the synthesis of diverse inorganic materials for both fundamental scientific investigations and industrial production. However, there are certain drawbacks associated with this approach, including high energy consumption, lack of uniformity in material composition, tendency for particle agglomeration, wide distribution of particle diameters, and a significant proportion of larger-sized grains. The synthesis of Na_xMnO_2 by applying the high-temperature solid phase method is mainly based on the uniform mixing of sodium source and manganese source according to the designed stoichiometric ratio, and the precursor preparation is formed through mechanical mixing. The chemical reaction of crystallization progress occurs under high-temperature conditions; finally, the Mn-based tunnel cathode material is obtained. By adjusting the synthesis parameters, Baudrin *et al.*[45] successfully prepared a highly crystalline pure $Na_{0.44}MnO_2$ cathode material using the solid-phase method. The specific procedure involved thoroughly grinding Na_2CO_3 and $MnCO_3$ in a mortar, followed by heating in air at 300 °C for 8 hours, and then at 800 °C for 9 hours with intermittent grinding. Electrochemical testing and *in situ* XRD technique characterization revealed significant changes in the polarization effect and specific capacity of the $Na_{0.44}MnO_2$ cathode during sodium ion insertion/removal progress. Avci *et al.*[48] utilized a mixture of Na_2O_2 and MnO_2, which were uniformly blended using an agate mortar in a glove box filled with Ar gas. The resulting mixture was then sintered at 750 °C for 24 hours in air. The growth of tunnel-structured nanorods initiates at 650 °C, with their orientation being perpendicular to the grain boundaries (Fig. 2(a)). Besides, it was observed that the presence of excess Na is crucial for the formation of rod-shaped tunnel structure $Na_{0.44}MnO_2$ (Fig. 2(b)).

3.2 Liquid-phase method

The sol–gel method involves the utilization of inorganic salts and other raw materials to dissolve them in a solution, form a sol, and then cure it into a gel. This process is employed to prepare precursors for cathode materials. Subsequently, these
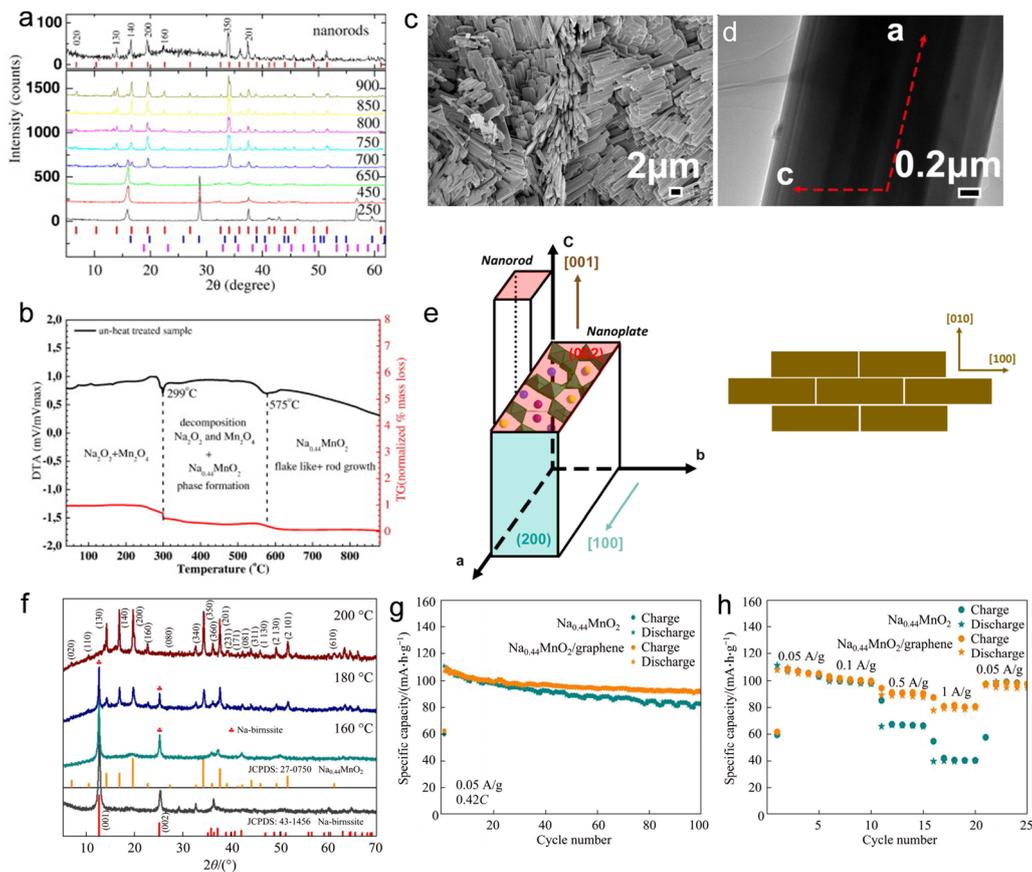
Fig. 2 (a) *Ex situ* XRD patterns of Na$_{0.44}$MnO$_2$ sample during heat treatment progress. (b) Differential thermal analysis (DTA) and thermogravimetric analysis (TG) data of the heating progress on the composition of Na$_2$O$_2$ and MnO$_2$. Reproduced with permission from ref. 48, Copyright (2015), Elsevier. (c) SEM image; (d) TEM image; and (e) schematic of the crystal particle growth and structure formation of nanorods and nanoplates. Reproduced with permission from ref. 49, Copyright (2016), Elsevier. (f) XRD patterns of tunnel-structured nanorods, Na$_{0.44}$MnO$_2$, prepared *via* hydrothermal synthesis at different hydrothermal reaction temperatures. The electrochemical performance of Na$_{0.44}$MnO$_2$/graphene and pristine Na$_{0.44}$MnO$_2$ cathode: (g) cycle performance at a current density of 50 mA g^{-1} and voltage range of 2.0–4.0 V; (h) rate capability. Reproduced with permission from ref. 50, Copyright (2019), Springer Nature.

precursors are subjected to heat treatment in a furnace, resulting in the desired chemical products. Utilizing the sol–gel method can effectively address the issue of the large grain size commonly encountered during solid-phase synthesis progress. Moreover, this approach enables the production of tunnel-type structure cathode materials with small particle sizes ranging from nanometers to microns. However, it is important to note that there are few drawbacks associated with synthesizing Mn-based tunnel cathode materials using the sol–gel method. These include higher costs due to expensive raw materials and the potential release of gases and organic compounds during both drying and high-temperature calcination processes, which may have adverse effects on environmental conditions in large-scale production. Xu and his colleagues[51] synthesized a Na$_{0.44}$MnO$_2$ cathode material with a unique morphology of elongated submicron slabs. Through precise control of the fabrication process and the use of specific chelating agents, they successfully manipulated the crystal structure and morphology of the resulting product. The resultant cathode material demonstrated exceptional dispersibility, ultra-long length, and significantly reduced thickness in the direction of sodium-ion deintercalation. Furthermore, the

cathode material prepared using this method exhibited a high capacity exceeding 120 mA h g^{-1}. Li *et al.*[49] successfully synthesized Na$_{0.44}$MnO$_2$ nanoplates with a monocrystalline orthorhombic structure using the sol–gel method assisted by templates. These nanoplates exhibited exceptional characteristics, such as high crystallinity, a pure phase, and a uniform size distribution (Fig. 2(c) and (d)). By subjecting polystyrene and citric acid to high-temperature calcination, a reductive carbothermal environment was created that effectively hindered the formation of one-dimensional particles and restricted particle growth along the [001] direction. The lamellar structure of Na$_{0.44}$MnO$_2$ material provided mechanical stability and facilitated short diffusion paths for efficient insertion/de-insertion of sodium ions due to its suitable channels and controlled morphology with limited crystal growth along the [001] direction (Fig. 2(e)).

The hydrothermal method is a widely utilized wet chemical synthesis method in which target products are synthesized under high temperature and high pressure by dissolving chemical raw materials in a solution. The particles of cathode materials produced using this method exhibit uniformity, and the morphology of the resulting products can be controlled by

adjusting reaction conditions and reactants. Additionally, the synthesized materials possess high purity. However, it should be noted that the hydrothermal method requires extensive reaction time, yields lower output, and necessitates advanced equipment, technology, and safety. In terms of synthesizing $Na_{0.44}MnO_2$ using a hydrothermal synthesis approach, soluble sodium salt and metallic manganese oxide serve as primary raw materials, while water or other solvents act as mediums for conducting chemical reactions within a high-pressure reactor. Wang et al.[50] successfully synthesized $Na_{0.44}MnO_2$ nanorods by optimizing the experimental parameters of the hydrothermal method (Fig. 2(f)). The conductivity of the material was increased by combining graphene with $Na_{0.44}MnO_2$ nanorods. $Na_{0.44}MnO_2$/graphene exhibits even better electrochemical performance, with an electrochemical discharge capacity of 106.9 mA h g^{-1} and superior rate capability. After 100 cycles, the capacity retention rate of the $Na_{0.44}MnO_2$/graphene cathode material reached 85.9% (Fig. 2(g) and (h)).

3.3 Other synthesis methods

In addition, some other preparation methods have been employed for the synthesis of Mn-based tunnel structure cathode materials, including the electrospinning technique, spray pyrolysis method, combustion method and molten salt method. Electrospinning is a flexible and practical method for producing fibers of varying diameters, ranging from nanometers to micrometers, with lengths that can extend up to kilometers. Wang et al.[52] reported the successful creation of two distinct hierarchical structures of $Na_{0.44}MnO_2$ using an optimized electrospinning technique, followed by controlled annealing processes. The structure consists of single-crystalline nanorods (NR) and demonstrates excellent cyclic stability, maintaining a reversible specific capacity of 120 mA h g^{-1} even after undergoing 140 cycles. However, the structure composed of nanofibers (NF) exhibits remarkable rate performance with a reversible specific capacity of 69.5 mA h g^{-1} at a high current density of 10C, which can be attributed to its unique one-dimensional ultralong and continuous fibrous network architecture. Axelbaum et al.[53] utilized a cost-effective and scalable technique, namely spray pyrolysis, to synthesize Na–Mn–O cathode material possessing tunnel structures. In the initial electrochemistry cycle, a discharge capacity of 115 mA h g^{-1} was achieved, while the material demonstrated favorable cycling stability and rate capability. Solution combustion synthesis is a highly promising technique for the controlled preparation of various functional oxide materials.[54] This method involves an exothermic and self-sustaining redox reaction, which occurs upon heating a mixture of aqueous metal nitrates and organic fuels, such as glycine and urea. Zhu et al.[55] successfully synthesized tunnel-structured $Na_{0.44}MnO_2$ using a simple and controllable solution combustion synthesis method, followed by the progress of calcination. The optimized $Na_{0.44}MnO_2$ electrode exhibited excellent electrochemical performance, including a high reversible capacity of 117 mA h g^{-1} at 0.1C, good rate capability, and outstanding cyclability with a high capacity retention of 100 mA h g^{-1} after undergoing 300 cycles at 4C rate. In addition, the synthesis of a high-performance $Na_{0.44}MnO_2$ cathode is attempted using molten salt chemistry.[56]

Na_2CO_3 and Mn_2O_3 are employed as reactants, while sodium chloride is utilized as the molten salt. The resulting product demonstrates exceptional long-term cycling stability, with a capacity retention rate of 85.4% after 500 cycles. This outstanding electrochemical performance is further confirmed through continuous cycling tests in full-cell, where the capacity retention rate remains at 80.5% after 300 cycles at a 1C rate. The future direction of development not only involves further investigating the mechanism of crystal structure and morphology transformation in the synthesis processes of reported methods on cathode materials but also entails exploring innovative synthesis strategies suitable for Mn-based tunnel structure cathode material preparation.

4. Modification strategy

### 4.1 Bulk phase structure doping

Although the Mn-based S-shaped tunnel structure cathode has higher crystal structure stability than the layer structure cathode, the long-term cycle process still faces the issue of discharge capacity attenuation.[32] The cell volume expansion caused by sodium ions entering the tunnel structure also leads to lattice changes and phase transitions in the Mn-based cathode material, making it challenging to achieve superior electrochemical stability. The continuous embedding/removal of sodium ions in the Mn-based tunnel cathode material, as well as the sodium-ion diffusion ability in the matrix framework of the tunnel-structure cathode material gradually reduces, restricting its specific capacity value and rate performance upon discharge progress. To address these issues, the ion doping strategy has been extensively adapted to reform the intrinsic crystal structure of tunnel-type architecture cathode materials and improve their corresponding electrochemical performance.

4.1.1 Transition metal site doping. Transition metal site doping is an effective strategy for enhancing the electrochemical properties of Mn-based tunnel cathode materials. To mitigate the negative impact on the electrochemical progress of tunnel cathode material $Na_{0.44}MnO_2$, in an early study by Zhou et al.,[31] Ti^{4+} was identified as a promising dopant candidate due to its similar valence state as Mn^{4+} in tunnel structure $Na_{0.44}MnO_2$. The researchers synthesized a new tunnel cathode material $Na_{0.61}Ti_{0.48}Mn_{0.52}O_2$ using the solid-phase method where approximately half of the manganese ion was replaced by titanium ion. The resulting cathode materials demonstrated a reversible discharge capacity of 86 mA h g^{-1} with an average voltage of 2.9 V, and the capacity retention rate reached 81% after 100 cycles. Wu et al.[47] discovered that the incorporation of titanium ions into cathode materials with an Mn-based tunnel structure not only enhances the diffusion ability of sodium ions but also mitigates lattice stress. The galvanostatic intermittent titration technique (GITT) test demonstrates a significant improvement in Na^+ diffusion dynamics upon the introduction of titanium into the crystal structure. Moreover, during the extraction/insertion process of Na^+, there is merely a minimal cell volume change of 5.26%, indicating its low-strain characteristics in Ti-substituted $Na_{0.44}Mn_{1-x}Ti_xO_2$ cathode materials. The material demonstrates

a remarkable capacity of 96 mA h g^{-1}, even under the condition of a high rate of 5C. Moreover, it exhibits exceptional cycling stability with an impressive retention rate of approximately 74% over 1000 cycles. Zhang et al.[57] employed 4d metal cation Zr ions to substitute Mn ions in the tunnel structure of Na$_{0.44}$MnO$_2$ for crystal structure optimization and electrochemical performance enhancement. The inclusion of Zr ions in Na$_{0.44}$Mn$_{0.98}$Zr$_{0.02}$O$_2$ samples with a tunnel structure results in an impressive initial discharge specific capacity of 112 mA h g^{-1} and significantly improves the Na$^+$ diffusion coefficient, thereby achieving excellent rate characteristics. In situ XRD analysis reveals that Zr-doped Na$_{0.44}$Mn$_{0.98}$Zr$_{0.02}$O$_2$ structures exhibit negligible cell volume changes within the charge and discharge range of 2.0–3.0 V. This experimental analysis highlights superior Na$^+$ diffusion kinetics and stable electrochemical cycling properties of tunnel structures doped with Zr 4d metal ions. To enhance the reversibility of electrochemical reactions and phase transitions of tunnel-structure cathode materials, Zhou et al.[58] introduced Mg^{2+} into the MnO5 square pyramidal hinge in the Na$_{0.44}$MnO$_2$. This Mg-doping modification improves Na$^+$ diffusion kinetics and reduces

the de-sodiation energy in the tunnel structure. The Mg-doping cathode Na$_{0.44}$Mn$_{0.95}$Mg$_{0.05}$O$_2$ can maintain 67% of the initial capacity retention after 800 cycles at 2C. X-Ray diffraction (XRD) and X-ray absorption spectroscopy (XAS) confirm the excellent reversibility of structure changes and charge compensation during electrochemical processes. The XRD analysis using synchrotron-based time-resolved techniques reveals that Na$_{0.44}$Mn$_{0.95}$Mg$_{0.05}$O$_2$ cathode has a single phase without intermediate phases during high-rate electrochemical processes, as depicted in Fig. 3(a), which distinguishes it from most Mn-based layer-structure cathode materials. In addition, the poor performance and stability of Na$_{0.44}$MnO$_2$ can be attributed to the presence of trivalent manganese ions with the Jahn–Teller effect. Wu et al.[59] effectively substituted trivalent iron ions for these trivalent manganese ions within the tunnel structure of Na$_{0.44}$MnO$_2$, resulting in a reduction in the Mn^{3+} to Mn^{4+} ratio and alleviating the negative impact of the Jahn–Teller effect on its electrochemical behavior as a cathode material with a tunnel structure (Fig. 3(b)). Raman spectroscopy and X-ray photoelectron spectroscopy (XPS) confirmed the partial replacement of trivalent manganese ions
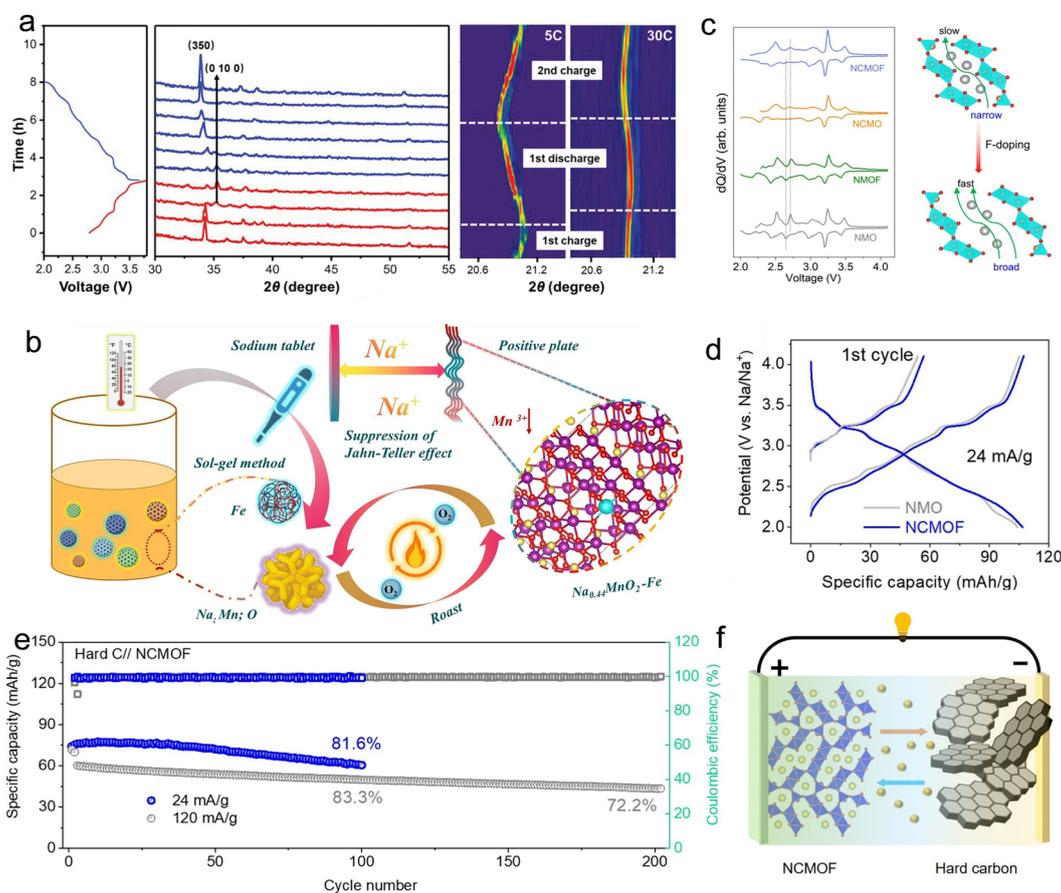
Fig. 3 (a) Ex situ XRD data of Mg-doped tunnel cathode during charge/discharge progress at 0.2C, 5C, and 30C. Reproduced with permission from ref. 58, Copyright (2021), Wiley-VCH. (b) Synthesis progress of Fe-doped tunnel cathode materials and systematic elucidation of the Fe doping mechanism. Reproduced with permission from ref. 59, Copyright (2024), Elsevier. (c) Boosting effect on the electrochemical property of synergetic anion–cation co-doping in Na$_{0.44}$MnO$_2$ tunnel-phase cathode. (d) Charge/discharge curves during the initial cycle in voltage ranging from 2.0 to 4.1 V. (e) Cycle performance of the full cell. (f) Schematic diagram of the assembled full cell by Cu/F co-doping tunnel cathode and hard carbon anode. Reproduced with permission from ref. 60, Copyright (2024), Elsevier.

with trivalent iron ions. The doped $Na_{0.44}Mn_{0.994}Fe_{0.006}O_2$ cathode material exhibits enhanced electrochemical kinetics, particularly evident in its rate performance at a reversible capacity of 87.9 mA h g^{-1} at 2C.

The cation co-doping methods were also employed to facilitate Na$^+$ insertion/extraction behavior and stabilize the tunnel crystal structure to further enhance its comprehensive electrochemical properties. Through the implementation of metal ion co-doping techniques, a favorable balance and enhancement in overall material properties encompassing structure, morphology, discharge capacity, cycle life, and rate performance are anticipated in the tunnel-type structure cathode. The Mg-doped Mn-based materials with a tunnel structure exhibit a higher discharge capacity than the original tunnel structure cathode, while non-electrochemically active Ti-doped tunnel structure materials sacrifice part of the electrochemically active element in favor of crystal structure stabilization, resulting in a lower initial discharge capacity. Remarkably, the synergistic effect of trace amounts of Mg and Ti leads to a more stable crystal structure and superior electrochemical performance of the co-doped cathode material $Na_{0.44}Mn_{0.895}Ti_{0.1}Mg_{0.005}O_2$. By simultaneously introducing magnesium ions and titanium ions into the crystal structure, it is possible to expand the cell lattice, resulting in enhanced structure stability, enlarged tunnel size, reduced length-to-diameter ratio for facilitating Na$^+$ insertion/extraction, and increased ion diffusion rate. The cathode $Na_{0.44}Mn_{0.895}Ti_{0.1}Mg_{0.005}O_2$ exhibits an impressive specific capacity of 80.0 mA h g^{-1} at a high rate of 20C, demonstrating a remarkable capacity retention rate of 67% even after the ultra-long cycle of 2000 times.[61] Qian's research group[62] introduced three kinds of metal elements (Al, Ti, and Co) into the Mn-ion sites simultaneously to form a medium-entropy substituted tunnel-type $Na_{0.44}Mn_{0.97}Al_{0.01}Ti_{0.01}Co_{0.01}O_2$ material. The medium-entropy substitution increases the spacing of lattice fringes and replaces Mn ions in the $Na_{0.44}MnO_2$ effectively. The optimized cathode material exhibits excellent rate performance, achieving a rated capacity of up to 80 mA h g^{-1} at 20C and maintaining a high capacity of 78 mA h g^{-1} after 2000 cycles at 10C.

4.1.2 Sodium-ion site doping.
Researchers have made efforts to control the occupancy of sodium ions within the Mn-based tunnel structure, aiming to regulate this ion site for outstanding electrochemical performance. The stoichiometry of sodium ions and other metal ion species/content at the sodium-ion site significantly affects the electrochemical performance of Na-containing compound electrode materials. In the initial research process on the tunnel-structure cathode material, B. Raveau et al.[63] successfully synthesized a cathode material, $Na_{1.1}Ca_{1.8}Mn_9O_{18}$, with Mn-based tunnel structure by incorporating Ca^{2+} into the sodium-ion vacancy of crystal texture, which has a similar ion radius as sodium ions but differs mainly in cationic deficiency, distribution and positions within the tunnels. Moreover, increasing sodium-ion content in Mn-based tunnel structures is employed to improve the electrochemical performance of Mn-based electrode material.[29] Liu et al.[64] reported a newly developed sodium-rich tunnel-type $Na_{0.6}MnO_2$ material, which was synthesized using a cetyltrimethylammonium bromide

(CTAB) surfactant as a template-assisted agent. The rapid diffusion kinetics and superior storage ability of Na$^+$ within the framework during charge/discharge progress were confirmed through GITT and ex situ XRD, respectively. Besides, other metal cations suitable for doping and occupying the sodium ion sites in the tunnel structure are also mapped. Wu et al.[65] introduced K ions with a larger radius than sodium ions into the Mn-based tunnel structure cathode material with an overall chemical composition of $Na_{0.5}K_{0.1}MnO_2$. However, its phase composition exhibited a composite structure consisting of $Na_4Mn_9O_{18}$ and KMn_8O_{16} phases. Despite this composite phase nature, it still demonstrated excellent electrochemical cycling stability and rate performance as a cathode material for SIBs. A discharge capacity of 82.2 mA h g^{-1} could be sustained for 300 cycles at a rate of 1C, and at a high rate of 4C, the cathode obtained over 70 mA h g^{-1}. Moreover, this material demonstrates an electrochemical capacity that exceeds the theoretical capacity of the tunnel structure, reaching an impressive value of 142.3 mA h g^{-1}. In future studies, introducing trace amounts ($<5\%$) of cations similar to or slightly larger than the radius of sodium ions into the Mn-based tunnel structure may play an important role in enhancing its structural stability and electrochemical performance.

4.1.3 Anion site doping.
In addition to the two cation sites occupied by the transition metal and sodium ion, some researchers have employed heterogeneous anions to modify the oxygen-anion sites within the Mn-based tunnel crystal texture.[66] Oxygen atoms play a crucial role in bridging atoms between pairs of transition metals, forming TM–O–TM interactions in transition metal oxide compounds. Anionic dopants often exert distance-dependent effects on specific properties at low doping concentrations. Zhou et al.[67] introduced higher electronegative fluorine ions into the Mn-based tunnel structure by doping to obtain a series of F-doped $Na_{0.66}[Mn_{0.66}Ti_{0.34}]O_{2-x}F_x$ ($x < 0.1$) tunnel structure cathode materials, resulting in increased sodium ion content in F-doped tunnel-type crystal structures due to the promotion effect of high-molar-ratio titanium ions on the thermodynamic stability of the tunnel structure. The optimized stoichiometry F-doped tunnel structure cathode $Na_{0.66}[M_{n0.66}Ti_{0.34}]O_{1.94}F_{0.06}$ exhibits a reversible capacity of 97 mA h g^{-1} along with a cycle performance to maintain 85 mA h g^{-1} at 2C after 100 cycles, accompanied by extremely low voltage polarization levels. Furthermore, the $Na_{0.66}[Mn_{0.66}Ti_{0.34}]O_{1.94}F_{0.06}$ cathode displays superior electrochemical performance under low-temperature conditions attributed to enhanced thermodynamics and kinetics resulting from fluorine doping. $Na_{0.66}[Mn_{0.66}Ti_{0.34}]O_{1.94}F_{0.06}$ cathode demonstrate a reversible capacity of 84 mA h g^{-1} at 0 °C and 61.5 mA h g^{-1} at −20 °C, respectively. In a subsequent study, Liu et al.[68] incorporated fluorine ions into pure Mn-based tunnel structure cathode material $Na_{0.44}MnO_2$ and observed the phase transition from the tunnel structure to the layer structure, resulting in the formation of a composite-structure cathode material with both tunnel and layer structure phases. A superior discharge capacity performance of 109 mA h g^{-1} is achieved at a high rate of 5C, demonstrating an impressive capacity retention of about 79%

even after 400 cycles. This finding demonstrates that F-substitution can effectively modify the tunnel-type structure and enhance its electrochemical activity, providing an exemplification for developing high-performance cathodes with composite structures for SIBs by introducing halogen anions as ion substitutes for lattice oxygen ions. In recent studies, a combination of cations and anions with different merits for crystal texture has been employed to enhance the electrochemical performance of tunnel structure cathode materials. Fu et al.[60] collaborated on anion–cation co-doping to modify the cathode material of an Mn-based tunnel structure by incorporating Cu^{2+} and F^- ions into the conventional tunnel-type cathode material $Na_{0.44}MnO_2$, aiming to break through the electrochemical property limitations. By preserving the intact crystal structure of the tunnel material, the robustness of the tunnel framework remains unaffected even after numerous cycles, ensuring a stable platform for the continuous extraction/insertion processes of Na^+ (Fig. 3(c) and (d)). The combination of anion–cation co-doping results in a synergistic effect, leading to improved Na^+ diffusion rate and highly stable cycling performance. Specifically, the capacity retentions after 150 cycles at the current density of 120 mA g^{-1} reach 98.9% and after 200 cycles at the current density of 360 mA g^{-1} can achieve 98.0%. The modified cathode material is combined with the hard carbon anode material to construct the full cell, as shown in Fig. 3(e) and (f), demonstrating capacity retention of 81.6% after 100 cycles and 72.2% after 200 cycles at a current density of 120 mA g^{-1}.

Although various heterogeneous ions are substituted at different ion sites in Mn-based tunnel-type cathode materials, the modified materials exhibit exceptional electrochemical performance. It is crucial to further comprehend the ion-doping mechanism for enhancing the crystal structure properties of Mn-based cathode materials and guiding the development of novel strategies for ion substitution modification strategy. Furthermore, unexplored elements can be employed for trace ion substitution to facilitate further investigation of modifications in the crystal structure and electrochemical properties.

4.2 Surface modification

Surface modification is a highly practical tailoring method for mitigating side reactions on the outer surface of cathode materials, effectively enhancing chemical stability and electrochemical properties. Park et al.[69] successfully designed and fabricated a relatively uniform dispersion of hybrid coating networks consisting of Al_2O_3 and MWCNTs onto the surface of tunnel-structure crystal particles, which exerted an inhibitory effect on the formation of damaging NaF-based solid–electrolyte interface, thereby facilitating rapid sodium ion transfer across the tunnel structure cathode/electrolyte interface. The rate capability and long-term cyclability of the tunnel-structure cathode were significantly enhanced through the incorporation of Al_2O_3/MWCNT. The upper limitation of the operating potential set for the tunnel-structure cathode in most previous studies is typically kept at about 4.0 V to prevent rapid discharge capacity degradation during cycle progress. Wang et al.[70] conducted a layer of Al_2O_3 coating on the surface of a tunnel-structure cathode to enhance its electrochemical properties at a high cut-off voltage.

The Al_2O_3-coated tunnel-structure cathode materials were prepared using a simple effective chemical coating method, and the corresponding coating amount was optimized to achieve this goal of enhancing high-voltage tolerance. The Al_2O_3-coated strategy effectively prevents the tunnel-structure cathode from undergoing direct contact reactions with the electrolyte and mitigating cell volume expansion during electrochemical processes. The resulting submicron rods with a 2 wt% Al_2O_3 coating exhibited increased electrochemical performance in the voltage range of 2.0–4.5 V, delivering an initial discharge capacity of 109.8 mA h g^{-1} at 0.4C and maintaining a capacity retention rate of 93.2% even after 200 cycles. Considering the analogous chemical properties between In_2O_3 and Al_2O_3, as well as its superior inertness and electrolyte resistance compared to Al_2O_3. Feng et al.[71] employed a precipitation method to coat In_2O_3 onto $Na_{0.44}MnO_2$ cathode material synthesized using a solid-state reaction method. Their findings demonstrate significant improvement in the electrochemical performance of 1 wt% In_2O_3-coated $Na_{0.44}MnO_2$, compared to pristine $Na_{0.44}MnO_2$, with an increase in capacity retention from 70.3% to 86.7% after cycling for 400 cycles at 1C under a high cut-off voltage of 4.5 V. These electrochemistry property enhancements can be attributed to the protective effect of In_2O_3 coating, which effectively mitigates undesired structure changes occurring during cycle processes and suppresses complex side reactions between the tunnel-structure cathode and electrolyte.

In addition to the conventional oxide coating tactics, Myung and his colleagues[72] propose a melt-impregnation technique at 350 °C to incorporate $(NH_4)_2MoO_4$ with unfavorable surface sodium residues on $Na_{0.44}MnO_2$ crystal particles, resulting in formatting an electro-conducting Na_2MoO_4 nanolayer on the tunnel-type $Na_{0.44}MnO_2$ compound's surface (Fig. 4(a)). The 1.5 wt% Na_2MoO_4-coated tunnel-structure cathode achieved long-term cycle stability at an ultra-high rate of 60C at the current density of 7.2 A g^{-1} and maintained a capacity of approximately 56 mA h g^{-1} without experiencing notable capacity decay for 1000 cycles (Fig. 4(b)). This remarkable cycle achievement can be attributed to the multifunctional effects of Na_2MoO_4 coating on the active compounds, facilitating electron transfer and providing protection coating against HF attack in the organic electrolyte environment during electrochemical reactions (Fig. 4(c)). In contrast, Huang et al.[73] adopted a different approach by utilizing a Na-rich layer oxide (Na_2TiO_3) as a multifunctional coating layer to modify the cathode material composed of tunnel-structure nanorods (Fig. 4(d)–(f)). The optimized 3 wt% Na_2TiO_3-coated $Na_{0.44}MnO_2$ exhibits an exceptionally high capacity-retention rate of up to 96.7%. Besides, this modified cathode exhibited ultra-stability rate cycle performance, achieving a capacity of 80.2 mA h g^{-1} at a rate of 20C and retaining 97.7% of its capacity after 900 cycles. Na_2TiO_3 coating acts as a reservoir for sodium ions and serves as an effective protective layer against electrolyte etching on the outer structure of $Na_{0.44}MnO_2$. Additionally, it should be noted that a 2D-layered Na_2TiO_3 coating functions to provide extra pathways other than [001] for sodium-ion diffusion along radial directions within nanorods, thereby reducing migration distances to
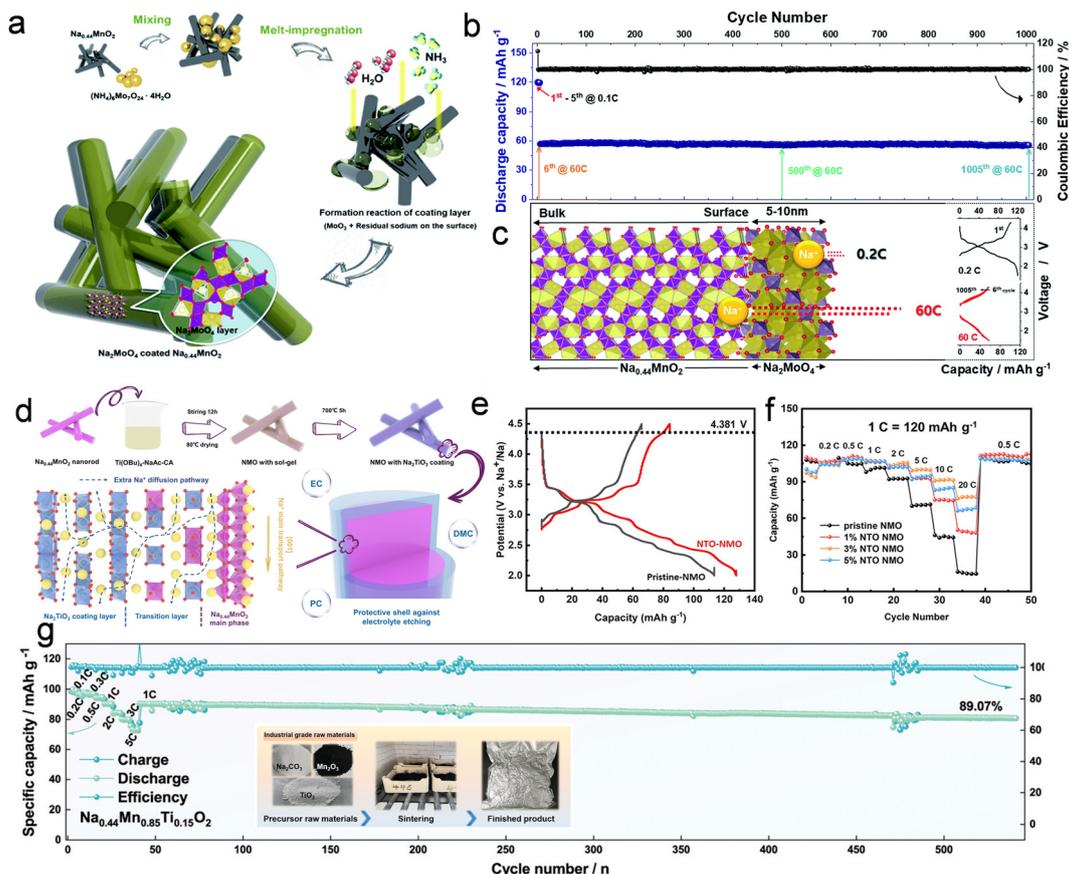
Fig. 4 (a) Formation process for the Na_2MoO_4 coating on the surface of crystal particle in $Na_{0.44}MnO_2$ cathode. (b) Initial 5 cycles at 0.1C and long-term cyclability performance at 60C for the coated tunnel-structure cathode $Na_{0.44}MnO_2$. (c) Schematic of sodium-ion transfer behavior through the Na_2MoO_4 coating layer during the charge/discharge process. Reproduced with permission from ref. 72, Copyright (2019), the Royal Society of Chemistry. (d) Synthesis process of Na_2TiO_3-coated tunnel-structure cathode. (e) Charge/discharge curves of pristine tunnel structure and 3 wt% Na_2TiO_3-coated tunnel structure cathode at 0.1C from 2 to 4.5 V. (f) Rate property of varying amounts of Na_2TiO_3-coated between 2 and 4.3 V. Reproduced with permission from ref. 73, Copyright (2023), the American Chemical Society. (g) Rate and cycle performance of industrial-grade cathode material $Na_{0.44}Mn_{0.85}Ti_{0.15}O_2$ and the inset graph corresponding to the optical picture of the industrial sample. Reproduced with permission from ref. 74, Copyright (2024), Wiley-VCH.

improve the rate performance of tunnel-structure compounds. Although the cathode material of the Mn-based tunnel structure exhibits favorable air stability, it is still susceptible to the side effects of surface residual alkali. In a recent investigation, Xiao et al.[74] successfully mitigated this issue by constructing a Ti-containing epitaxial stabilization layer. Meanwhile, they prepared a substantial quantity of industrial-grade $Na_{0.44}Mn_{0.85}Ti_{0.15}O_2$, and the assembled coin full cell and 18 650 battery retained superior electrochemical properties (Fig. 4(g)). Although surface modification has yielded favorable results in enhancing the properties of Mn-based tunnel-structure cathode materials, the current range of reported coating materials and specific coating method remains limited. Therefore, it is imperative to utilize experiments and theoretical calculations to explore some new coating agents to potentially uncover unforeseen enhancements in electrochemical properties.

4.3 Composite structure construction

Although the Mn-based tunnel structure cathode material offers outstanding structural stability and electrochemical cycle stability, its sodium-ion storage capacity is relatively lower than that of the Mn-based layer-type structure cathode. To address this property limitation, a composite phase cathode material with a combined Mn-based layer-structure $Na_{0.7}MnO_2$ with high capacity and tunnel-structure $Na_{0.44}MnO_2$ with high cycle stability has been developed to obtain a synergistic effect.[75,76] The reported literature presents two main distinct approaches for obtaining such layer-tunnel composite structure cathode materials: (1) the incorporation of heterogeneous ions into the Mn-based tunnel structure material leads to a partial transformation of tunnel-type structure into a layer-type structure during synthesis progress, resulting in the final formation of a hybrid phase consisting of both tunnel and layer structures. (2) Meticulous design of an appropriate sodium-ion content within the layer-tunnel composite structure and subsequent necessary modifications accordingly.

Chen et al.[77] synthesized a series of $Na_{0.44}Mn_{1-x}Co_xO_2$ cathode materials by doping Co^{3+}, resulting in Co^{3+} substitution into a tunnel-structure cathode for a lower ratio of Mn^{3+}. It was observed that an increase in Co content with a strong

preference for octahedral coordination ions led to a transition from a tunnel structure to a layer structure and the formation of a layer-tunnel composite structure. The part of the tunnel-type crystal structure could transform into the P2-type layer structure when the sodium content is 0.44 in $Na_{0.44}Mn_{0.92}Co_{0.08}O_2$ compound, with further increase in Co content for $Na_{0.44}Mn_{0.89}Co_{0.11}O_2$ compound, in which the P2 layer structure would be more thermodynamically stable in the final chemical product. Subsequently, the same research team introduced nickel ions and magnesium ions into the Mn-ion site of the tunnel structure $Na_{0.44}MnO_2$.[78] It was observed that as the introduction of nickel ions or magnesium ions increased in the structure, the Mn-based tunnel structure underwent a crystal structure transformation into a layer structure. Within a certain range of heterogeneous metal ion contents, a stabilized layer-tunnel composite structure can be achieved using a conventional thermopolymerization method. The specific discharge capacity of $Na_{0.44}Mn_{0.89}Mg_{0.11}O_2$ with tunnel-layer hybrid phase composition can achieve 188 mA h g^{-1} within the voltage range of 2.0–4.2 V at 0.1C, exhibiting a capacity retention of 81% after 70 cycles. Nickel-ion or magnesium-ion substitutions result in smoother charge/discharge curves compared to that of $Na_{0.44}MnO_2$ and can significantly enhance the overall capacity albeit with a slight reduction in specific capacity retention when compared to the pristine tunnel-structure cathode. Avci et al.[79] synthesized a composite-phase material by substituting trace amounts of Co into $Na_{0.44}MnO_2$, resulting in a layer-tunnel composite phase cathode ($Na_{0.44}MnO_2/Na_{0.7}MnO_{2.05}$) that effectively prevents phase transformations and structure degradation for superior electrochemical performance. The 1% Co-substituted composite material alleviates the Jahn–Teller effect and significantly improves the stability of its crystal structure. Furthermore, the same research team created another series of tunnel/P2 hybrid structures through a one-step heat treatment with Ni substitution at Mn sites.[80] These structures maintained high cycling stability and Coulombic efficiency similar to pristine T-$Na_{0.44}MnO_2$ while suppressing phase transition during charge/discharge cycles, ultimately resulting in superior cycling performance. Electrochemical analysis reveals that $Na_{0.44}MnO_2$ exhibits a capacity retention of 77% after 100 cycles at a rate of 0.3C, while Ni-substituted cathode materials demonstrate capacity retentions of approximately 86.4% and 77.3%.

Cao[81] then introduced a small amount of high-valence tungsten (W) ions into $Na_{0.44}MnO_2$, resulting in the efficient conversion of the tunnel structure to the layer structure for the first time. Compared with other reported doped metal ions, W ions can induce the phase transformation of $Na_{0.44}MnO_2$ at a relatively low doping concentration. When the proportion of tungsten (W) in the total amount of transition metal achieves 1%, the tunnel structure $Na_{0.44}MnO_2$ undergoes a phase transformation, which is fully converted to pure P2-layer $Na_{0.44}Mn_{0.99}W_{0.01}O_2$ during synthesis, demonstrating an enhanced reversible capacity of 195.5 mA h g^{-1}, along with exceptional cycling stability for capacity retention of 80% after 200 cycles. This provides a novel approach for engineering transition metal oxides to induce the conversion

from tunnel structure to layer structure. In addition to metal–cation substitution, Liu et al.[68] also systematically explored and investigated the introduction of fluorine ions into the structural oxygen in Mn-based tunnel structure cathode materials. They found that $Na_{0.44}MnO_{1.93}F_{0.07}$ cathode exhibited a layer structure and tunnel structure composite phase within the temperature range of 800–1100 °C after optimizing temperature conditions to obtain cathode materials with relatively superior electrochemical performance. The optimized $Na_{0.44}MnO_{1.93}F_{0.07}$ cathode exhibits higher electrochemical activity than that of the primary tunnel-phase cathode $Na_{0.44}MnO_2$, resulting in an exceptional discharge capacity of 149 mA h g^{-1} at a rate of 0.5C. Furthermore, the cathode demonstrates remarkable cycling stability with a capacity retention of around 79% over 400 cycles at a rate of 5C.

In addition to the aforementioned crystal structure transformation from an Mn-based tunnel structure to a layer structure, this results in the easy formation of the cathode material in the layer-tunnel composite structure. The Na/TM ratio is commonly 0.44 in the Mn-based tunnel structure, which enhances the thermodynamic stability of the tunnel structure during formation. Meanwhile, the Na/TM ratio in Mn-based layer oxide structures typically ranges around 0.7, making it easier to form a composite structure consisting of both layer and tunnel structures by directly setting the Na/TM ratio between 0.4 and 0.70.[16,82] In 2017, Wu et al.[83] successfully constructed a layer-tunnel composite cathode material $Na_{0.6}MnO_2$ by carefully designing a Na–Mn–O system cathode material with a Na/Mn ratio of 0.6, which exhibited excellent electrochemical performance. The underlying mechanism of the layer-tunnel composite structure cathode material is also elucidated (Fig. 5(a) and (b)). Subsequent studies regulated the composition ratio of layer-tunnel composite structures through metal Ni-ion substitution.[84] Additionally, other transition metal ions, such as Cu,[85] Fe,[86] Zr[87] and Mg,[88] have been explored owing to their application as substitution ions for Mn-ion sites or Na-ion sites in layer-tunnel composite structure research. Xiao et al.[89] utilized the thermal polymerization technique combined with the solid-state method to fabricate cathode materials featuring a composite structure of layer-tunnel intergrowth. The well-established layer-tunnel intergrowth structure cathode exhibited a satisfying reversible discharge capacity of 198.2 mA h g^{-1} at a rate of 0.2C, resulting in a remarkable high-energy density of 520.4 W h kg^{-1}. Wang et al.[90] investigated the regulatory mechanism of different elements on cathode materials with layer-tunnel composite structures and found that introducing iron ions promoted an increase in the proportion of layer structures, while titanium-ion introduction increased the proportion of tunnel structure within layer-tunnel composites. Introducing equal proportions of iron ions and titanium ions still facilitated transformation from layer to tunnel structure during the high-temperature calcination synthesis stage (Fig. 5(c)). This further indicates that different metal ions exhibit certain variances in regulating the layer-tunnel composite structure cathode materials, which can enable targeted phase regulation by utilizing distinct metal ions into the crystal texture. Since then, some studies on the design and construction of the particle layers of layer-tunnel cathode materials have been reported.[91] In a recent
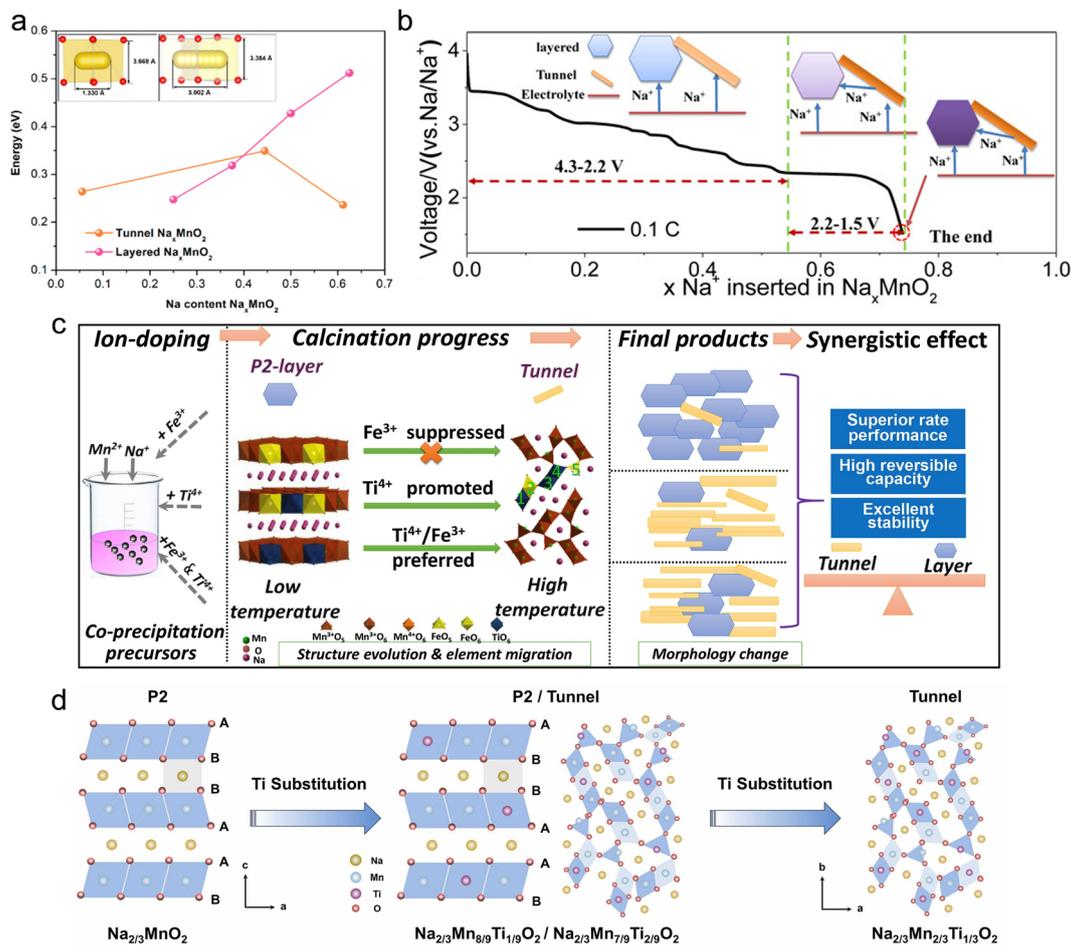
Fig. 5 (a) Sodium-ion migration barriers and the distance between oxygen and sodium migration in tunnel-type structure and layer-type structure Na_xMnO_2. (b) Schematic of the synergistic effect of the layer–tunnel composite structure. Reproduced with permission from ref. 83, Copyright (2017), the American Chemical Society. (c) Fe/Ti-ion doping induced a crystal structure formation process to achieve controlled synthesis of the layer–tunnel composite structure cathode. Reproduced with permission from ref. 90, Copyright (2020), Elsevier. (d) Schematic of the dynamic evolution of the atomic arrangement for $Na_{2/3}Mn_{1-x}Ti_xO_2$ cathode materials with different Ti-ion contents. Reproduced with permission from ref. 92, Copyright (2024), Elsevier.

study, Xiao et al.[92] successfully prepared a range of Ti-substituted $Na_{2/3}Mn_{1-x}Ti_xO_2$ cathode materials by manipulating the dynamic structural evolution, leading to a transition from the P2-$Na_{2/3}MnO_2$ layered structure to tunnel structure with increasing Ti-ion content (Fig. 5(d)). The optimized Ti-substituted cathode material $Na_{2/3}Mn_{8/9}Ti_{1/9}O_2$ demonstrated a discharge capacity of 202.9 mA h g^{-1} at 0.1C within a voltage range of 1.5–4.3 V, resulting in an energy density of 536.6 W h kg^{-1} and exhibiting 71.0% capacity retention after undergoing 300 cycles at 1C. Furthermore, advanced characterization techniques, including in situ XRD analysis, confirmed a highly reversible phase transition process between P2/tunnel-OP4/tunnel structures and an interlocking effect between the layer and tunnel structures as well as remarkable moisture stability even after exposure to water treatment.

Overall, significant progress has been made in layer–tunnel composite structure cathode materials, especially because breaking through the theoretical capacity of the original tunnel structure cathode materials is not sufficiently high. Some more accurate tuning strategies for tunnel–layer composite structure

cathode materials need to be further developed, and in-depth studies in this area have great research potential. The modification strategies extensively utilized for cathode materials featuring an Mn-based tunnel structure $Na_{0.44}MnO_2$ are comprehensively illustrated in Fig. 6.

5. Conclusion and perspective

Due to the promising application prospects of SIBs in large-scale energy storage systems and the substantial market demand in the near future, the research and development of high-performance and cost-effective cathode materials will play a pivotal role in optimizing both the overall cost and performance of SIBs. As a potential candidate for cathode material, Mn-based tunnel structure cathode material $Na_{0.44}MnO_2$ possesses remarkable advantages, such as exceptional stability, high-power output, and low production costs. Despite significant progress achieved in developing SIBs utilizing Mn-based tunnel-structure cathode materials, there is still room for
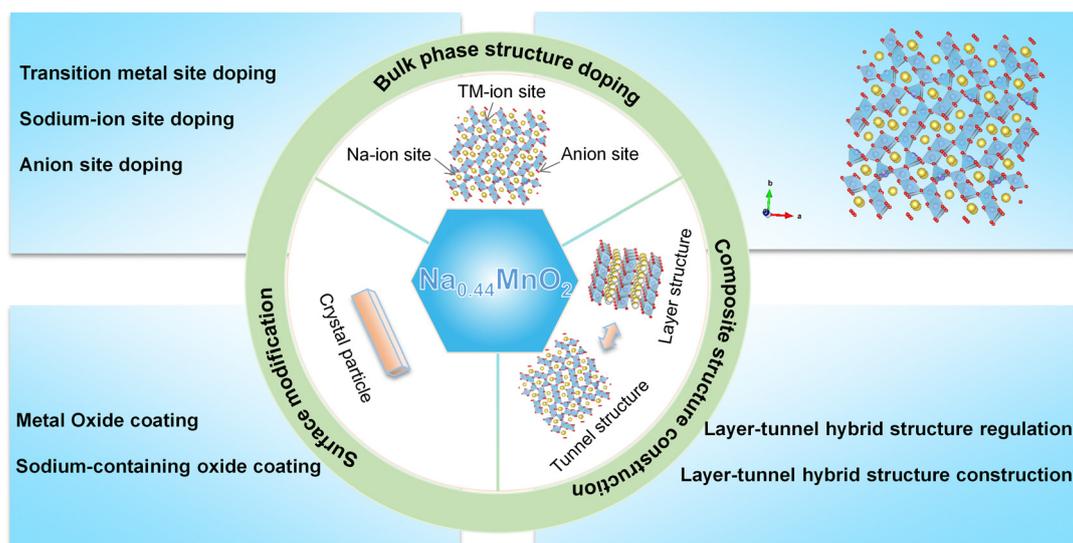
Fig. 6 Summary diagram of the modification strategies for tunnel-structured Na$_{0.44}$MnO$_2$ cathode material in SIBs.

further improvement and enhancement of their inherent merits, including a stable crystal structure, outstanding cycle durability, and impressive rate capability. However, challenges such as insufficient specific capacity persist, resulting from limited sodium-ion mobility within the intrinsic structure, instability of the crystal structure over extended cycles, and capacity degradation caused by the Jahn–Teller effect. In this comprehensive review article, we systematically summarize and discuss various aspects related to electrochemical sodium-ion storage mechanisms and controlled synthesis techniques for material fabrication, and modification strategies employed for Mn-based tunnel structures and propose some potential directions for future research trends.

Overall, the future research and development of tunnel structure cathode materials can be concentrated on the following aspects: (1) developing more effective modification strategies to mitigate the impact of the Jahn–Teller effect on trivalent manganese ions within the tunnel structure, while optimizing the surface structure of crystal particles to control the formation of inactive substances. Further utilization of versatile characterization strategies and research methodologies is vital for elucidating the underlying electrochemical mechanisms of these modification methods, thereby facilitating the attainment of more stable crystal structures and enhanced electrochemical properties. (2) Designing high-sodium-content Mn-based cathode materials or exploring additional sodium sources for chemical pre-sodiation solutions to compensate for insufficient sodium-ion content in tunnel-structure cathodes can enhance the initial Coulomb efficiency when directly assembling a full cell with a hard carbon anode. Alternatively, conducting a targeted search for chemically presodiated hard carbon anodes that exhibit good compatibility with the cathode material of the Mn-based tunnel structure can further optimize the first Coulomb efficiency in the full cell, thereby maintaining the specific discharge capacity performance of the tunnel-structure cathode materials. (3) Developing scalable synthesis strategies for producing Mn-based tunnel-type

cathode materials with a stable crystal structure and uniform morphological characteristics, which contribute to improved electrochemical performance and cost reduction. These efforts will facilitate the development of low-cost Mn-based tunnel-structure cathode materials from fundamental research to practical industry applications.

Data availability

No primary research results, software or code have been included and no new data were generated or analyzed as part of this review.

Conflicts of interest

There are no conflicts to declare.

Acknowledgements

Notes and references

1 Z. W. Yang Yang, C. Du, B. Wang, X. Li, S. Wu, X. Li, X. Zhang, X. Wang, Yaoshen Niu, Feixiang Ding, Xiaohui Rong, Yaxiang Lu, Nian Zhang, Jg Xu, Ruijuan Xiao, Qinghua Zhang, Xuefeng Wang, Wen Yin, J. Zhao, Liquan Chen, Jianyu Huang and Yong-Sheng Hu, *Science*, 2024, **385**, 744–752.
2 X. Jin, X. Zhang, P. Zhang, S. Rohani, H. Li, M. He, L. Teng, Q. Liu and W. Liu, *Hydrometallurgy*, 2024, **224**, 106243.
3 C. Zhao, Q. Wang, Z. Yao, J. Wang, B. Sánchez-Lengeling, F. Ding, X. Qi, Y. Lu, X. Bai, B. Li, H. Li, A. Aspuru-Guzik, X. Huang,

C. Delmas, M. Wagemaker, L. Chen and Y. S. Hu, *Science*, 2020, **370**, 708–711.

4 M. He, W. Liu and Z. Yang, *Chem. Commun.*, 2023, **59**, 10785–10788.

5 M. He, X. Jin, X. Zhang, X. Duan, P. Zhang, L. Teng, Q. Liu and W. Liu, *Green Chem.*, 2023, **25**, 6561–6580.

6 M. He, X. Zhang, H. Li, X. Jin, L. Teng, Q. Liu and W. Liu, *J. Environ. Chem. Eng.*, 2023, **11**, 111099.

7 Y. Liu, D. Wang, H. Li, P. Li, Y. Sun, Y. Liu, Y. Liu, B. Zhong, Z. Wu and X. Guo, *J. Mater. Chem. A*, 2022, **10**, 3869–3888.

8 S. Jia, S. Kumakura and E. McCalla, *Energy Environ. Sci.*, 2024, **17**, 4343–4389.

9 D. Wang, C. Zhu, Y. Liu, C. Hu, H. Yang, Z. Li, T. Chen, B. Zhong, Z. Wu and X. Guo, *ACS Appl. Mater. Interfaces*, 2024, **16**, 24442–24452.

10 R. Umezawa, Y. Tsuchiya, T. Ishigaki, H. B. Rajendra and N. Yabuuchi, *Chem. Commun.*, 2021, **57**, 2756–2759.

11 Y. Liang, H. Xu, K. Jiang, J. Bian, S. Guo and H. Zhou, *Chem. Commun.*, 2021, **57**, 2891–2894.

12 J. Wang, Y. F. Zhu, Y. Su, J. X. Guo, S. Chen, H. K. Liu, S. X. Dou, S. L. Chou and Y. Xiao, *Chem. Soc. Rev.*, 2024, **53**, 4230–4301.

13 N. Zhang, X. Dong, Q. Yan, J. Wang, F. Jin, J. Liu, D. Wang, H. Liu, B. Wang and S. Dou, *Energy Storage Mater.*, 2024, **72**, 103734.

14 X. Zhou, J. Hu, S. Ajmal, D. Xiang, Z. Sun, W. Chen, M. Zhu, P. Chen and P. Li, *Chem. Commun.*, 2023, **59**, 12152–12155.

15 B. J. Xin and X. L. Wu, *Battery Energy*, 2024, **3**, 20230074.

16 D. Wang, Y. H. Liu, Z. G. Wu, Y. L. Liu, C. Q. Zhu, B. H. Zhong and X. D. Guo, *Chem. Eng. J.*, 2023, **462**, 141994.

17 T. Zhang, M. Ren, Y. Huang, F. Li, W. Hua, S. Indris and F. Li, *Angew. Chem., Int. Ed.*, 2024, **63**, e202316949.

18 D. Wang, Y. Liu, Z. Wu, X. Liu, J. Qu, H. Liu, Y. Ming, Y. Zhong, B. Zhong and X. Guo, *Chem. Commun.*, 2020, **56**, 2921–2924.

19 J. Liu, W. Huang, R. Liu, J. Lang, Y. Li, T. Liu, K. Amine and H. Li, *Adv. Funct. Mater.*, 2024, **34**, 2315437.

20 K. H. Wong, M. Zhang, T. Yang, Q. Ma, S. Dai, J. Wei, G. K. Veerasubramani, A. A. AlHammadi, G. Karanikolos, E. Bekyarova, A. Elkamel and A. Yu, *Energy Storage Mater.*, 2024, **71**, 103549.

21 H. Hirsh, M. Olguin, H. Chung, Y. Li, S. Bai, D. Feng, D. Wang, M. Zhang and Y. S. Meng, *J. Electrochem. Soc.*, 2019, **166**, A2528–A2535.

22 Y. Wang, T. Yang, J. Liu, T. Zhang, Y. Zhang, Y. Gao, Z. Sun, S. Jia, L. Yang and Z. Chen, *Nano Energy*, 2024, **131**, 110260.

23 Y. Cao, M. Xiao, X. Sun, W. Dong and F. Huang, *Chemistry*, 2023, **29**, e202202997.

24 J. Feng, S. Luo, K. Cai, S. Yan, Q. Wang, Y. Zhang and X. Liu, *Chin. Chem. Lett.*, 2022, **33**, 2316–2326.

25 Y. Wang, L. Mu, J. Liu, Z. Yang, X. Yu, L. Gu, Y. S. Hu, H. Li, X. Q. Yang, L. Chen and X. Huang, *Adv. Energy Mater.*, 2015, **5**, 1501005.

26 C. Liu, L. Jia, J. Li, Y. Wu and B. Zhang, *Mater. Lett.*, 2022, **308**, 131102.

27 R. O. Jean-Paul Parant, M. Devalette, C. Fouassier and E. Paul Hagenmuller, *J. Solid State Chem.*, 1971, **3**, 1–11.

28 M. Y. P. Marca, M. Doeff, Y. Ma and L. C. De Jonghe, *J. Electrochem. Soc.*, 1994, **141**, 145–147.

29 S. Xu, Y. Wang, L. Ben, Y. Lyu, N. Song, Z. Yang, Y. Li, L. Mu, H. T. Yang, L. Gu, Y. S. Hu, H. Li, Z. H. Cheng, L. Chen and X. Huang, *Adv. Energy Mater.*, 2015, **5**, 1501156.

30 X. Zhang, J. Chen, J. Ye, T. Zhang and Z. Hou, *Adv. Energy Mater.*, 2023, **13**, 2204413.

31 S. Guo, H. Yu, D. Liu, W. Tian, X. Liu, N. Hanada, M. Ishida and H. Zhou, *Chem. Commun.*, 2014, **50**, 7998–8001.

32 W.-J. Shi, H.-X. Li, D. Zhang, F.-H. Du, Y.-H. Zhang, Z.-Y. Wang, X.-H. Zhang and P.-F. Zhang, *Chem. Eng. J.*, 2023, **477**, 146976.

33 C. H. Rim, C. H. Jang, K. H. Kim, C. Ryu and C. J. Yu, *Phys. Chem. Chem. Phys.*, 2022, **24**, 22736–22745.

34 S. Chakrabarty, J. A. Dar, A. Joshi, A. Paperni, S. Taragin, A. Maddegalla, G. Sai Gautam, A. Mukherjee and M. Noked, *J. Mater. Chem. A*, 2024, **12**, 25109.

35 B. Mandal, S. Chakrabarti and A. K. Thakur, *Comput. Mater. Sci.*, 2024, **238**, 112934.

36 S. Maddukuri, A. Nimkar, M. S. Chae, T. R. Penki, S. Luski and D. Aurbach, *Front. Energy Res.*, 2021, **8**, 615677.

37 Z. Guo, Y. Zhao, Y. Ding, X. Dong, L. Chen, J. Cao, C. Wang, Y. Xia, H. Peng and Y. Wang, *Chem*, 2017, **3**, 348–362.

38 K. Wang, G. Guo, X. Tan, L. Zheng and H. Zhang, *Chem. Eng. J.*, 2023, **451**, 139059.

39 M. Soleimanzade, M. Radaelli, J. Manidi, M. Bahdanchyk and A. Vicenzo, *Batteries*, 2023, **9**, 428.

40 M. S. Chae, Y. Elias and D. Aurbach, *ChemElectroChem*, 2021, **8**, 798–811.

41 H. Kim, D. J. Kim, D.-H. Seo, M. S. Yeom, K. Kang, D. K. Kim and Y. Jung, *Chem. Mater.*, 2012, **24**, 1205–1211.

42 R. Qiao, K. Dai, J. Mao, T.-C. Weng, D. Sokaras, D. Nordlund, X. Song, V. S. Battaglia, Z. Hussain, G. Liu and W. Yang, *Nano Energy*, 2015, **16**, 186–195.

43 M. S. Chae, H. J. Kim, H. Bu, J. Lyoo, R. Attias, B. Dlugatch, M. Oliel, Y. Gofer, S. T. Hong and D. Aurbach, *Adv. Energy Mater.*, 2020, **10**, 2000564.

44 Q. Liu, Z. Hu, M. Chen, Q. Gu, Y. Dou, Z. Sun, S. Chou and S. X. Dou, *ACS Appl. Mater. Interfaces*, 2017, **9**, 3644–3652.

45 L. F. F. Sauvage, J.-M. Tarascon and E. Baudrin, *Inorg. Chem.*, 2007, **46**, 3289–3294.

46 D. J. Kim, R. Ponraj, A. G. Kannan, H.-W. Lee, R. Fathi, R. Ruffo, C. M. Mari and D. K. Kim, *J. Power Sources*, 2013, **244**, 758–763.

47 W. J. Shi, D. Zhang, X. M. Meng, C. X. Bao, S. D. Xu, L. Chen, X. M. Wang, S. B. Liu and Y. C. Wu, *ACS Appl. Mater. Interfaces*, 2020, **12**, 14174–14184.

48 S. Demirel, E. Oz, E. Altin, S. Altin, A. Bayri, P. Kaya, S. Turan and S. Avci, *Mater. Charact.*, 2015, **105**, 104–112.

49 X. He, J. Wang, B. Qiu, E. Paillard, C. Ma, X. Cao, H. Liu, M. C. Stan, H. Liu, T. Gallash, Y. S. Meng and J. Li, *Nano Energy*, 2016, **27**, 602–610.

50 Y. Zheng, Y. Ouyang, L. Liu, J. Xia, S. Nie, W. Liu and X.-Y. Wang, *J. Cent. South Univ.*, 2019, **26**, 1510–1520.

51 M. Xu, Y. Niu, C. Chen, J. Song, S. Bao and C. M. Li, *RSC Adv.*, 2014, **4**, 38140–38143.

52 B. Fu, X. Zhou and Y. Wang, *J. Power Sources*, 2016, **310**, 102–108.

53 K.-Y. Shen, M. Lengyel, L. Wang and R. L. Axelbaum, *MRS Commun.*, 2017, **7**, 74–77.

54 C. Ferrara, C. Tealdi, V. Dall'Asta, D. Buchholz, L. Chagas, E. Quartarone, V. Berbenni and S. Passerini, *Batteries*, 2018, **4**, 8.

55 N. Sheng, C.-g Han, Y. Lei and C. Zhu, *Electrochim. Acta*, 2018, **283**, 1560–1567.

56 H. Zhao, L. Wu, J. Tian, D. Zhang, X. Li, S. Xu, L. Chen, Q. Yi, K. Dai and H. Guo, *New J. Chem.*, 2023, **47**, 3892–3902.

57 W.-J. Shi, Y.-M. Zheng, X.-M. Meng, S.-B. Liu, S.-D. Xu, L. Chen, X.-M. Wang and D. Zhang, *ChemElectroChem*, 2021, **8**, 798–811.

58 X. L. Li, J. Bao, Y. F. Li, D. Chen, C. Ma, Q. Q. Qiu, X. Y. Yue, Q. C. Wang and Y. N. Zhou, *Adv. Sci.*, 2021, **8**, 2004448.

59 H. Zhang, Y. Xiang, B. Liu, G. Li, C. Dun, H. Huang, Q. Zou, L. Xiong and X. Wu, *J. Colloid Interface Sci.*, 2024, **661**, 389–400.

60 T. Cui, X. Li, Y. Si and Y. Fu, *Energy Storage Mater.*, 2024, **65**, 103161.

61 H. Zhonge, J. Yuxuan, J. Wang, L. Yuhua, Z. Wenqing, J. Hongyuqi, S. Yongqiang, W. Xianwen and X. Yanhong, *J. Solid State Chem.*, 2024, **329**, 124415.

62 J. Chen, Z. Hou, L. Zhang, W. Mao, T. Zhang, X. Zhang and Y. Qian, *Inorg. Chem. Front.*, 2023, **10**, 841–849.

63 N. Floros, C. Michel, M. Hervieu and B. Raveau, *J. Solid State Chem.*, 2001, **162**, 34–41.

64 J. Zhang, H. Yuan, Y. Huang, S. Kan, Y. Wu, M. Bu, Y. Liu, P. He and H. Liu, *Chem. Eng. J.*, 2021, **417**, 128097.

65 Z.-G. Wu, Y.-J. Zhong, J.-T. Li, K. Wang, X.-D. Guo, L. Huang, B.-H. Zhong and S.-G. Sun, *RSC Adv.*, 2016, **6**, 54404–54409.

66 R. Ruiz, C. Perez-Vicente and R. Alcantara, *Dalton Trans.*, 2024, **53**, 4814–4822.

67 Q.-C. Wang, Q.-Q. Qiu, N. Xiao, Z.-W. Fu, X.-J. Wu, X.-Q. Yang and Y.-N. Zhou, *Energy Storage Mater.*, 2018, **15**, 1–7.

68 W.-J. Shi, Y.-W. Yan, C. Chi, X.-T. Ma, D. Zhang, S.-D. Xu, L. Chen, X.-M. Wang and S.-B. Liu, *J. Power Sources*, 2019, **427**, 129–137.

69 T.-E. Fan, S.-M. Liu, X. Tang, Z.-H. Zou, J.-Q. Xie and M.-Y. Wang, *Ionics*, 2021, **27**, 1137–1142.

70 Y. Zhang, L. Liu, S. Jamil, J. Xie, W. Liu, J. Xia, S. Nie and X. Wang, *Appl. Surf. Sci.*, 2019, **494**, 1156–1165.

71 W. Liu, Q. Ren, M. Yang, L. Liu, Y. Zhang, D. Su, J. Wen, Q. Wang, X. Wang and Y. Feng, *J. Alloys Compd.*, 2022, **896**, 163087.

72 J. U. Choi, J. H. Jo, C.-H. Jo, M. K. Cho, Y. J. Park, Y. Jin, H. Yashiro and S.-T. Myung, *J. Mater. Chem. A*, 2019, **7**, 13522–13530.

73 Y. Cao, M. Xiao, W. Dong, T. Cai, T. Gao, H. Bi and F. Huang, *ACS Appl. Mater. Interfaces*, 2023, **15**, 40469–40477.

74 H. Liu, L. Kong, H. Wang, J. Li, J. Wang, Y. Zhu, H. Li, Z. Jian, X. Jia, Y. Su, S. Zhang, J. Mao, S. Chen, Y. Liu, S. Chou and Y. Xiao, *Adv. Mater.*, 2024, e2407994, DOI: **10.1002/adma.202407994**.

75 Y. Su, N. N. Zhang, J. Y. Li, Y. Liu, H. Y. Hu, J. Wang, H. Li, L. Y. Kong, X. B. Jia, Y. F. Zhu, S. Chen, J. Z. Wang, S. X. Dou, S. Chou and Y. Xiao, *ACS Appl. Mater. Interfaces*, 2023, **15**, 44839–44847.

76 J. Wang, Q.-Q. Sun, J. Yu, J.-X. Guo, N.-K. Mo, H.-W. Li, Y. Su, S. Zhao, Y.-F. Zhu, H. Chu, S. Dou and Y. Xiao, *Composites, Part B*, 2024, **284**, 111664.

77 Y.-T. Zhou, X. Sun, B.-K. Zou, J.-Y. Liao, Z.-Y. Wen and C.-H. Chen, *Electrochim. Acta*, 2016, **213**, 496–503.

78 Y. Shao, Y.-T. Zhou, M.-M. Deng, Z.-F. Tang, J.-Y. Liao, H. J. M. Bouwmeester and C.-H. Chen, *J. Solid State Electrochem.*, 2019, **23**, 2979–2988.

79 E. Oz, S. Altin and S. Avci, *ACS Omega*, 2023, **8**, 27170–27178.

80 E. Oz, S. Altin and S. Avci, *J. Solid State Chem.*, 2023, **318**, 123741.

81 Q. Ding, W. Zheng, A. Zhao, Y. Zhao, K. Chen, X. Zhou, H. Zhang, Q. Li, X. Ai, H. Yang, Y. Fang and Y. Cao, *Adv. Energy Mater.*, 2023, **13**, 2203802.

82 T.-R. Chen, Z.-G. Wu, W. Xiang, E.-H. Wang, C.-J. Wu, M.-Z. Chen, X.-D. Guo and B.-H. Zhong, *Ceram. Int.*, 2017, **43**, 6303–6311.

83 Z. G. Wu, J. T. Li, Y. J. Zhong, X. D. Guo, L. Huang, B. H. Zhong, D. A. Agyeman, J. M. Lim, D. H. Kim, M. H. Cho and Y. M. Kang, *ACS Appl. Mater. Interfaces*, 2017, **9**, 21267–21275.

84 H. Chen, Z. Wu, Z. Zheng, T. Chen, X. Guo, J. Li and B. Zhong, *Electrochim. Acta*, 2018, **273**, 63–70.

85 T. R. Chen, T. Sheng, Z. G. Wu, J. T. Li, E. H. Wang, C. J. Wu, H. T. Li, X. D. Guo, B. H. Zhong, L. Huang and S. G. Sun, *ACS Appl. Mater. Interfaces*, 2018, **10**, 10147–10156.

86 Z. Sun, B. Peng, L. Zhao, J. Li, L. Shi and G. Zhang, *Energy Storage Mater.*, 2021, **40**, 320–328.

87 J. Qu, T. Sheng, Z.-G. Wu, T.-R. Chen, H. Chen, Z.-G. Yang, X.-D. Guo, J.-T. Li, B.-H. Zhong and X.-S. Dou, *J. Mater. Chem. A*, 2018, **6**, 13934–13942.

88 J. Qu, D. Wang, Z. G. Yang, Z. G. Wu, L. Qiu, X. D. Guo, J. T. Li, B. H. Zhong, X. C. Chen and S. X. Dou, *ACS Appl. Mater. Interfaces*, 2019, **11**, 26938–26945.

89 Y. Xiao, P. F. Wang, Y. X. Yin, Y. F. Zhu, X. Yang, X. D. Zhang, Y. Wang, X. D. Guo, B. H. Zhong and Y. G. Guo, *Adv. Energy Mater.*, 2018, **8**, 1800492.

90 D. Wang, C. Shi, Y.-P. Deng, Z. Wu, Z. Yang, Y. Zhong, Y. Jiang, B. Zhong, L. Huang, X. Guo and Z. Chen, *Nano Energy*, 2020, **70**, 104539.

91 D. Wang, Y.-P. Deng, Y. Liu, Y. Jiang, B. Zhong, Z. Wu, X. Guo and Z. Chen, *Nano Energy*, 2023, **110**, 108340.

92 Z.-C. Jian, Y.-F. Liu, Y.-F. Zhu, J.-Y. Li, H.-Y. Hu, J. Wang, L.-Y. Kong, X.-B. Jia, H.-X. Liu, J.-X. Guo, M.-Y. Li, Y.-S. Xu, J.-F. Mao, S.-L. Zhang, Y. Su, S.-X. Dou, S.-L. Chou and Y. Xiao, *Nano Energy*, 2024, **125**, 109528.